

Sub-10-nm graphene nanoribbons with atomically smooth edges from squashed carbon nanotubes

Changxin Chen ^{1,2,14}, Yu Lin ^{3,14}, Wu Zhou ^{4,5,14}, Ming Gong², Zhuoyang He¹, Fangyuan Shi¹, Xinyue Li¹, Justin Zachary Wu², Kai Tak Lam⁶, Jian Nong Wangˀ, Fan Yang՞, Qiaoshi Zeng ^{9,10}, Jing Guo⁶, Wenpei Gao¹¹, Jian-Min Zuo ¹¹¹, Jie Liu ¹², Guosong Hong ¹², Alexander L. Antaris², Meng-Chang Lin¹³, Wendy L. Mao ³³,8 and Hongjie Dai ³² ≥

Graphene nanoribbons are of potential use in the development of electronic and optoelectronic devices. However, the preparation of narrow and long nanoribbons with smooth edges, sizeable bandgaps and high mobilities is challenging. Here we show that sub-10-nm-wide semiconducting graphene nanoribbons with atomically smooth closed edges can be produced by squashing carbon nanotubes using a high-pressure and thermal treatment. With this approach, nanoribbons as narrow as 1.4 nm can be created, and up to 54% of single- and double-walled nanotubes in a sample can be converted into edge-closed nanoribbons. We also fabricate edge-opened nanoribbons using nitric acid as the oxidant to selectively etch the edges of the squashed nanotubes under high pressure. A field-effect transistor fabricated using a 2.8-nm-wide edge-closed nanoribbon exhibits an on/off current ratio of more than 10⁴, from which a bandgap of around 494 meV is estimated. The device also exhibits a field-effect mobility of 2,443 cm² V⁻¹ s⁻¹ and an on-state channel conductivity of 7.42 mS.

he use of two-dimensional graphene in electronics and optoelectronics is limited because the material has a zero bandgap¹. One solution is to use one-dimensional graphene nanoribbons (GNRs)². Theoretical^{3,4} and experimental⁵⁻⁷ studies have shown that GNRs with widths less than 10 nm become semiconducting due to quantum confinement and edge effects. They exhibit a bandgap that scales inversely with their widths, which depend on edge chiralities as well as the family types of armchair GNRs^{3,4,8,9}. In particular, GNRs with widths under 5 nm can have sizeable bandgaps^{5,6,10}. Narrow GNRs also have an advantage over single-walled carbon nanotubes (SWCNTs) in the development of all-semiconducting devices (for example, use in integrated circuits), because it is challenging to obtain 100% semiconducting SWCNTs using present separation or growth technology. The mobility and conductivity of GNRs are highly dependent on the degree of edge roughness due to edge-scattering effects¹¹⁻¹³. To fabricate high-performance electronic and optoelectronic devices, narrow and long GNRs with smooth edges throughout the whole ribbon are required.

Methods of preparing GNRs wider than 10 nm include electron-beam lithography¹⁴, unzipping multi-walled carbon nanotubes (MWCNTs)^{7,15-17}, chemical vapour deposition (CVD)¹⁸ and epitaxial synthesis on semiconductor substrates¹⁹. GNRs narrower than 10 nm have been prepared by the sonochemical exfoliation of

expandable graphite⁶, gas-phase etching of wide GNRs²⁰, patterning of two-dimensional graphene using a nanowire mask²¹, catalytic unzipping of SWCNTs²² and scanning tunnelling microscopy lithography²³. However, these approaches produce GNRs with large defect densities or roughness at their edges, as well as non-uniform edge structures, which substantially decrease mobility. Edge variation between GNRs also causes large differences in electronic structure and properties.

Approaches using bottom-up solution synthesis can provide soluble and narrow GNRs (1 nm to several nanometres in width)^{24,25} but with relatively short lengths, varying from several nanometres to 200 nm, which leads to contact lengths that are shorter than the transfer length (0.2-0.5 µm) and insufficient for making low-impedance contacts²⁶⁻²⁸. In addition, long and dense functional groups attached to the GNR's cove-type periphery can increase the scattering effects and decrease mobility. It is possible to produce GNRs that are only a few atoms wide with chemically smooth edges using a surface-assisted assembly method²⁹⁻³¹, but these nanoribbons are also typically short (of the order of dozens of nanometres) and have low mobility. This assembly is usually performed on a specific crystal plane of a conductive single-crystal metal, so an additional substrate transfer step is needed for device implementation, which could result in structural damages to GNRs. Recently, seven-atom-wide GNRs were formed on a semiconducting metal

National Key Laboratory of Science and Technology on Micro/Nano Fabrication, Key Laboratory for Thin Film and Microfabrication of Ministry of Education, Department of Micro/Nano Electronics, School of Electronic Information and Electrical Engineering, Shanghai Jiao Tong University, Shanghai, China. ²Department of Chemistry, Stanford University, Stanford, CA, USA. ³Stanford Institute for Materials and Energy Sciences, SLAC National Accelerator Laboratory, Menlo Park, CA, USA. ⁴Materials Science and Technology Division, Oak Ridge National Laboratory, Oak Ridge, TN, USA. ⁵School of Physical Sciences and CAS Center for Excellence in Topological Quantum Computation, University of Chinese Academy of Sciences, Beijing, China. ⁶Department of Electrical and Computer Engineering, University of Florida, Gainesville, FL, USA. ⁷School of Materials Science and Engineering, East China University of Science and Technology, Shanghai, China. ⁸Department of Geological Sciences, Stanford University, Stanford, CA, USA. ⁹Center for High Pressure Science and Technology Advanced Research, Shanghai, China. ¹⁰Jiangsu Key Laboratory of Advanced Metallic Materials, School of Materials Science and Engineering, Southeast University, Nanjing, China. ¹¹Department of Materials Science and Engineering, University of Illinois at Urbana-Champaign, Urbana, IL, USA. ¹²Department of Chemistry, Duke University, Durham, NC, USA. ¹³College of Electrical Engineering and Automation, Shandong University of Science and Technology, Qingdao, China. ¹⁴These authors contributed equally: Changxin Chen, Yu Lin, Wu Zhou. ⁵⁸e-mail: chen.c.x@sjtu.edu.cn; wmao@stanford.edu; hdai@stanford.edu

oxide (TiO_2) surface using an on-surface synthesis approach³². However, the length of the prepared GNRs was only about 10 nm and the synthesis required ultrahigh-vacuum conditions.

In this Article, we show that sub-10-nm-wide and long GNRs with atomically smooth closed edges can be produced by irreversibly squashing carbon nanotubes (CNTs) using a high-pressure and thermal treatment. With this approach, we create sub-5-nm GNRs, with the narrowest width of 1.4 nm. The quality of the resulting GNRs is assessed with scanning transmission electron microscopy (STEM) and Raman spectroscopy mapping. For CNTs with a diameter ranging from 1.9 to 6.4 nm, the yield for squashing SWCNTs and double-walled carbon nanotubes (DWCNTs) into edge-closed GNRs is estimated to be 54%. We also prepare edge-opened GNRs by selectively etching the edges of squashed CNTs at a high pressure using an oxidant (nitric acid; HNO₃). A field-effect transistor (FET) fabricated using an edge-closed 2.8-nm-wide GNR from a squashed DWCNT exhibits an on/off current ratio (I_{on}/I_{off}) of more than 104, estimated bandgap of 494 meV, on-state channel conductivity of $7.42\,\text{mS}$ and field-effect mobility of $2,443\,\text{cm}^2\,\text{V}^{-1}\,\text{s}^{-1}$. An FET with a 9.9-nm-wide GNR channel exhibits a device mobility of 3,776 cm² V⁻¹ s⁻¹.

Squashing CNTs into GNRs via pressure and thermal treatment

We studied two types of CNT sample. Sample 1 was purified large-diameter CNTs with the main diameter ranging from 1.9 to 6.4 nm centred at around 3.7 nm and was synthesized via a floating-catalyst CVD method³³, where $70\pm5\%$ of the CNTs were SWCNTs and DWCNTs and the remaining were few-walled CNTs. Sample 2 was purified CNTs with the main diameter ranging from 0.8 to 3.0 nm and was prepared via the catalyst-supported CVD method³⁴, which was mostly composed of DWCNTs and small quantities of single- and tri-walled CNTs (Methods provides more details).

A diamond anvil cell (DAC) was used for the high-pressure treatment of CNTs. The CNT samples were loaded (to fill) and sealed in a sample chamber in the centre of a pre-indented tungsten gasket that was then compressed between two diamond anvils (Supplementary Fig. 1 and Methods). The sample chamber has a height of about 70 μm and a diameter of 410 μm . Figure 1a illustrates the structural change in CNTs before and after the high-pressure and thermal treatment, where the pristine CNTs (left) are squashed into GNRs (right) after treatment.

The structural evolution of Sample 1 from ambient pressure to 22.8 GPa was monitored by in situ Raman spectroscopy through the diamond window (Methods). Under atmospheric pressure, a resonant radial breathing mode (RBM) peak at 116 cm⁻¹ was observed, corresponding to CNTs with a diameter of ~2.1 nm. With increasing pressure, the RBM blueshifts and the peak intensity decreases (Fig. 1b, left). The RBM was nearly invisible when the pressure reached 5.5 GPa. The shift and disappearance of the RBM was attributed to the radial structural transition occurring in CNTs under high pressure, which modifies their sub-band energy gaps. Eventually, this change prevents the excitation laser from resonating with the sub-bands. Previous theoretical studies on ideal and defect-free CNTs under increased hydrostatic pressure showed that the radial cross-section of a CNT would transform from a circle into an ellipse and then into a peanut shape before it finally collapsed, and the collapse pressure was dependent on the CNT diameter^{35–37}. The calculation showed that a CNT with a diameter of 0.8 nm collapsed under a hydrostatic pressure of about 6.8 GPa (ref. 36). In our experiment, a relatively higher pressure of 22.8 GPa was applied and no pressure-transmitting medium was used, which resulted in the introduction of deviatoric stress. This would allow CNTs to be squashed more readily. Moreover, CVD-synthesized CNTs used in our experiment had structural defects on the tube walls, which

made our CNTs more susceptible to deformation than the ideal and defect-free ones studied in the theoretical calculations.

Similarly, the G-band was also observed to blueshift and the intensity decreased with increasing pressure (Fig. 1c, left). The blueshift was $60 \, \text{cm}^{-1}$ when the pressure was increased from the ambient value to $20.9 \, \text{GPa}$. The blueshift of the G-band could be attributed to the shortening of the C–C bonds under pressure, which strengthened the bonds and increased the vibrational frequency¹⁰. We also observed a change in the rate of G-band shift near $4.0 \, \text{GPa}$ (Fig. 1d). Together with the disappearance of the RBM, a notable radial structural transition can be deduced to occur in Sample 1 near $4.0 \, \text{GPa}$ (ref. 36).

To stabilize the squashed sample structure, we conducted an annealing process on the sample at the highest pressure of 22.8 GPa. The sample was first heated up to 220 °C and kept for 40 min. Then, the sample was cooled down to room temperature under a rapid airflow. After unloading the DAC back to ambient pressure, there was no obvious recovery of the RBM peak (Fig. 1b, right), indicating that a majority of CNTs underwent irreversible radial deformation. The Raman G-band of the sample gradually shifted back to the lower wavenumber as the pressure decreased (Fig. 1c, right), which suggested that the C-C-bond length was restored after releasing the pressure. Different from the compression process, a much smaller change in the rate of G-band shift was observed near 2.8 GPa along decompression (Fig. 1d), which indicated that only a small number of CNTs regained their original shape from radial deformation after the pressure was released. Compared with pristine CNTs, the sample after the high-pressure and thermal treatment had a weaker (that is, more obtuse) G-band (Fig. 1c). This might be because the prepared GNRs from squashed CNTs have a lower degree of graphitization compared with their parent CNTs due to the formed edges. STEM characterization, which will be discussed later, showed that the edge regions of the prepared GNRs have a larger layer spacing between the two innermost layers than the middle plane, whose interlayer spacing approximates that of ideal graphite. This results in a lower degree of graphitization in the edge regions and reduces the total degree of graphitization for the prepared GNRs. In our approach, the application of a high non-hydrostatic pressure and suitable thermal treatment along with the stabilizing effect of innate defects in CNTs contribute to the realization of irreversible radial deformation.

We also observed that the D-to-G intensity ratio increased after the high-pressure treatment by comparing the Raman spectra of Sample 1 before and after the pressure and thermal treatment (Fig. 1e). The increase in D-to-G intensity ratio can be mainly attributed to the presence of edges^{38,39}, which indicates that CNTs are squashed to form GNRs. It is also likely that some lattice deformation occurs at the edges in the squashed CNTs after the high-pressure treatment. Both of them can break the vibrational symmetry of the lattice to significantly increase the D-mode intensity⁴⁰ and therefore enhance the D-to-G intensity ratio.

Previous studies on seven-atom-wide and nine-atom-wide armchair GNRs prepared via on-surface synthesis showed a low-frequency radial-breathing-like mode (RBLM) in the Raman spectra using 532 and 785 nm excitation lasers, respectively ^{39,41,42}. This is because the RBLM of GNRs is coherently excited by photon energies near the lowest optical transition ⁴³. In contrast, no RBLM was observed for treated Sample 1 or 2 under high pressure using 532, 633 or 785 nm excitation lasers. This can be attributed to these excitation energies being far away from the bandgaps of the resulting GNRs so that the RBLM cannot be resonantly excited. Although we did not observe the RBLM, the shift and irreversible disappearance of the RBM for CNTs, increase in the D-to-G intensity ratio and change in the rate of G-band shift along compression and decompression indicated that the radial cross-section of CNTs had experienced a significant irreversible transformation.

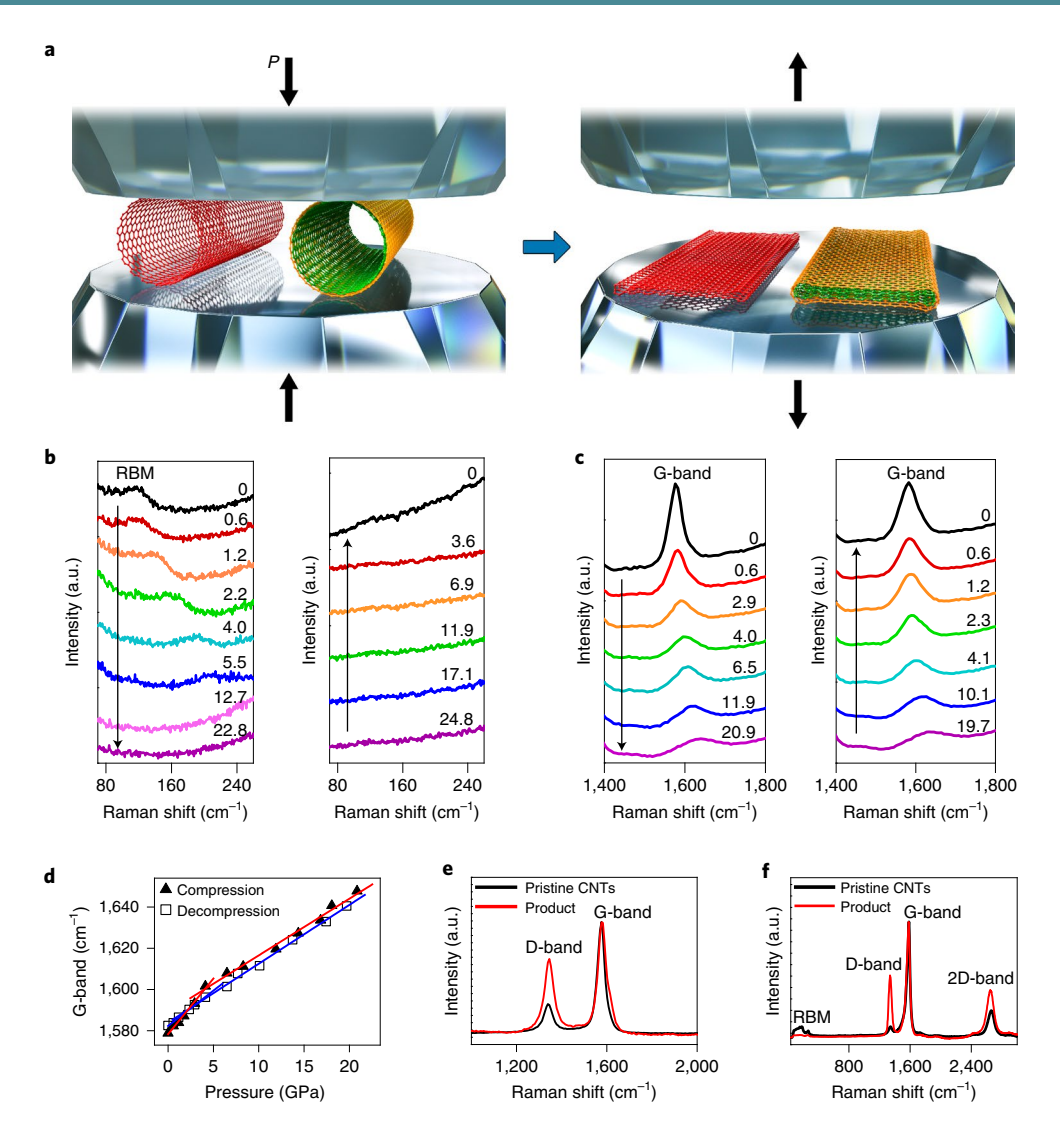


Fig. 1 In situ Raman measurements of the samples undergoing a high-pressure and thermal treatment in a DAC. **a**, Schematic of squashing an SWCNT and DWCNT (left) into edge-closed double-layer and four-layer GNRs (right) via a high-pressure (*P*) and thermal treatment. One SWCNT and one DWCNT (left) are shown to represent the CNT samples used in the experiments. The black arrows show the movement directions of the diamond anvils. **b,c**, Raman spectra showing the evolution of the RBM (**b**) and G-band (**c**) for Sample 1 with gradual pressure loading (left) and unloading (right). Arrows indicate the pressure pathways. Pressure is in the unit of GPa and '0 GPa' denotes the atmospheric pressure. The left and right plots in **b** and **c** have the same value range in the *y* axis. **d**, Evolution of the G-band as a function of pressure for Sample 1 along the compression and decompression processes. On compression, the G-band shows a blueshift at a rate of 5.4 cm⁻¹ GPa⁻¹ below 4.0 GPa and a much-reduced rate of 2.8 cm⁻¹ GPa⁻¹ above 4.0 GPa, as indicated by the fitting lines shown in red. Along decompression, the change in the rate of the G-band shift is much smaller. The fitting lines (shown in blue) of the decompression points indicate a shift rate of 2.9 cm⁻¹ GPa⁻¹ above 2.8 GPa followed by a shift rate of 3.4 cm⁻¹ GPa⁻¹ below 2.8 GPa. **e**, Raman spectra of Sample 1 before and after the pressure and thermal treatment. **f**, Raman spectra of Sample 2 before and after the pressure and thermal treatment. The two spectra in **e** and **f** were taken before loading pressure and after releasing pressure, respectively, with the DAC open, which were plotted with normalized G-band intensities.

Sample 2, which has a smaller diameter than Sample 1, was compressed up to a pressure of 28.1 GPa and comparable Raman results were obtained (Supplementary Fig. 2). After releasing the pressure, the RBM peaks at 155 and 188 cm⁻¹ corresponding to CNTs with a diameter of 1.6 and 1.3 nm, respectively, had no obvious recovery, while a minor RBM peak at 266 cm⁻¹ corresponding to the smaller CNTs with a diameter of 0.9 nm was recovered (Fig. 1f and Supplementary Fig. 2a,b). This indicates that a small portion of smaller-diameter CNTs in Sample 2 can restore their original radial shape after the pressure cycle. More in situ high-pressure Raman measurements were also conducted on the CNT samples prepared by an arc-discharge method (Supplementary Fig. 3). Similar to Sample 1, we also observed the disappearance of RBM and the increase in D-to-G intensity ratio after decompression.

Electron microscopy characterization of GNRs

Transmission electron microscopy (TEM) and STEM characterizations of the recovered samples from the DACs after the high-pressure and thermal treatments showed the presence of both GNRs and CNTs in the products (Methods). Figure 2 shows the images of some GNRs from squashed CNTs in treated Samples 1 and 2. In contrast to CNTs (Fig. 2a, top, and Supplementary Fig. 4a), GNRs exhibited a much lower image contrast between the edge and middle planes (Fig. 2a, bottom, Fig. 2b and Supplementary Fig. 4b,c), which is attributed to their flat configuration. Besides flat GNRs, twisted (Fig. 2c-f and Supplementary Fig. 4d-f) and folded (Fig. 2i) GNRs were also observed. The GNR width observed in treated Sample 1 mainly ranges from 2.8 to 10 nm. In treated Sample 2, sub-5-nm GNRs ranging from 1.4 to 4.7 nm could be observed.

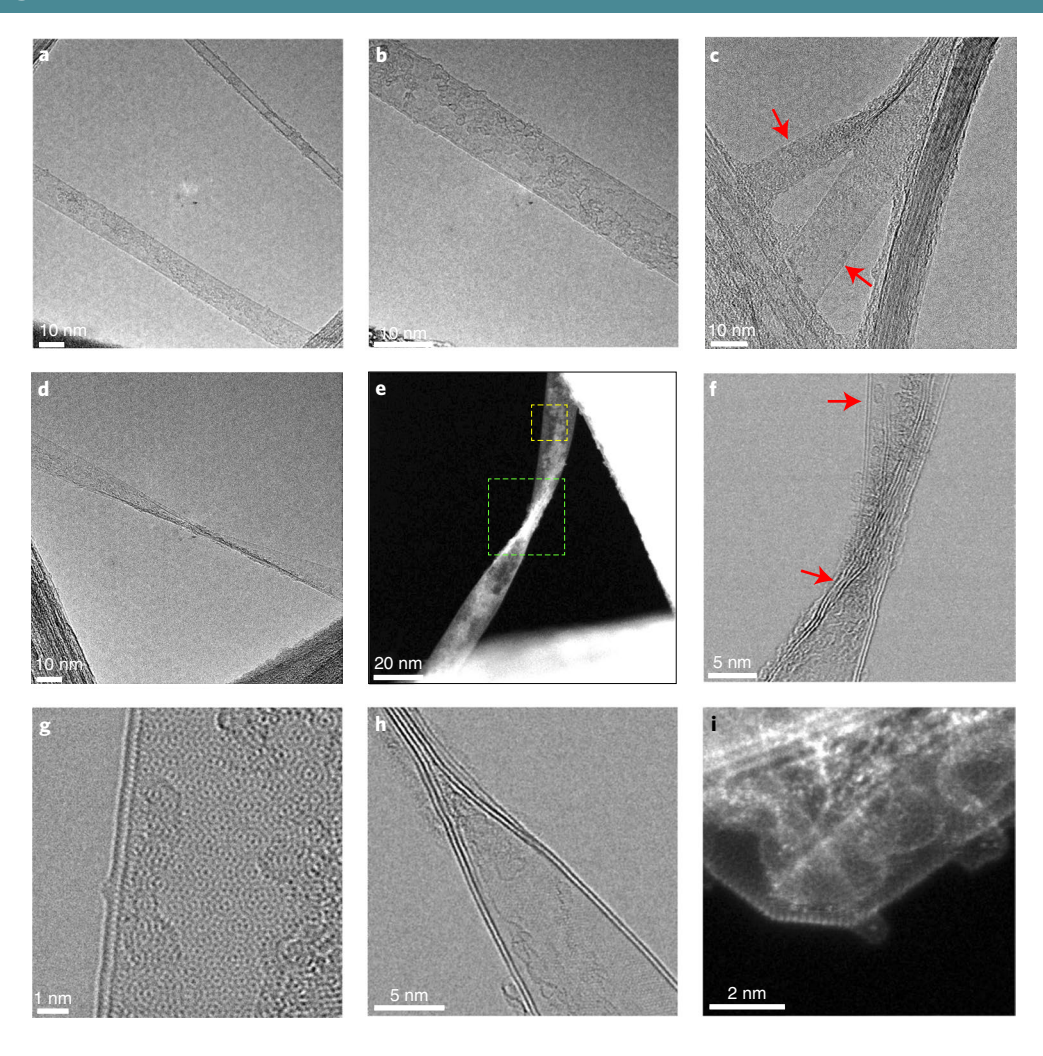


Fig. 2 | TEM and STEM images of GNRs from squashed CNTs. a, TEM image showing a four-layer GNR (bottom) and a DWCNT (top). The GNR has less contrast between the edge and middle planes than the CNT. **b**, Zoomed-in TEM image of the GNR in **a. c**, TEM image of a twisted four-layer GNR (top arrow) and a flat four-layer GNR (bottom arrow). **d**, TEM image of a twisted double-layer GNR. **e**, STEM-ADF *Z*-contrast image of a twisted four-layer GNR. **f,g**, Zoomed-in STEM-BF phase-contrast images of the twisted (**f**) and flat (**g**) regions in **e**, which were taken from the green and yellow squares in **e**, respectively. In **f**, four graphene layers can be observed when the observation direction is parallel to the GNR plane (bottom arrow) and two walls can be observed when the observation direction is perpendicular to the GNR plane (top arrow). **h**, STEM-BF phase-contrast image of a structure with part of the DWCNT squashed into the four-layer GNR. **i**, STEM-ADF *Z*-contrast image of a folded double-layer GNR with a width of 2.6 ± 0.3 nm. **a-h** were taken from treated Sample 1; **i** was taken from treated Sample 2.

The length of the prepared GNRs is typically larger than 1 µm and can reach several micrometres according to the atomic force microscopy (AFM) measurements on the straight GNRs. Figure 2e shows the STEM annular dark-field (ADF) Z-contrast image of a twisted four-layer GNR showing that the CNT was squashed after the high-pressure treatment. From the zoomed-in STEM bright-field (BF) phase-contrast image of the twisted region of the GNR (Fig. 2f), we can clearly observe four graphene layers in this GNR (marked by the bottom arrow in Fig. 2f) and deduce that this GNR is derived from a squashed DWCNT, which is consistent with the observed number of walls of the GNR's edge (marked by the top arrow in Fig. 2f). In the zoomed-in STEM-BF image for the flat region of this GNR, the moiré patterns in the central region of the GNR and close to the edge of the GNR are uniform, and both central and edge regions of the GNR are in focus (Fig. 2g), which indicate that this sample has a flat configuration (Supplementary Note 1). A small number of CNTs are shown to be partially squashed into GNRs (Fig. 2h and Supplementary Fig. 4h,g). Figure 2i shows an atomic-resolution STEM image of a folded GNR with a narrow width of 2.6 ± 0.3 nm in treated Sample 2.

Figure 3a and Supplementary Fig. 5 show a typical sub-10-nm edge-closed GNR with a width of 9.2 nm from treated Sample 1. The atomic-resolution STEM-BF image (Fig. 3b) and STEM-ADF image (Fig. 3c) demonstrate a uniform moiré pattern with the central region and edge region concurrently in focus. In contrast, the atomic-resolution STEM-BF (Fig. 3i) and STEM-ADF (Fig. 3j) images of a CNT show different moiré patterns with changes in the focal plane of the edge and central regions. STEM-ADF data offer an intensity map. The intensity profile of the ADF image for the GNR in Fig. 3c is nearly flat in the central region with slightly higher values near the edge (Fig. 3d). The CNT in Fig. 3j has an obvious 'U'-shaped intensity profile of the ADF image (Fig. 3k). These results are confirmed by the simulation of the scattering potentials and ADF image intensities of the edge-closed GNR and CNT via QSTEM software (Supplementary Fig. 6 and Methods). The difference in the scattering potential and ADF image intensity between a CNT and an edge-closed GNR is also qualitatively explained in Supplementary Note 2.

It is also observed that GNRs have different fast Fourier transform (FFT) patterns from the central and edge regions of their STEM-BF

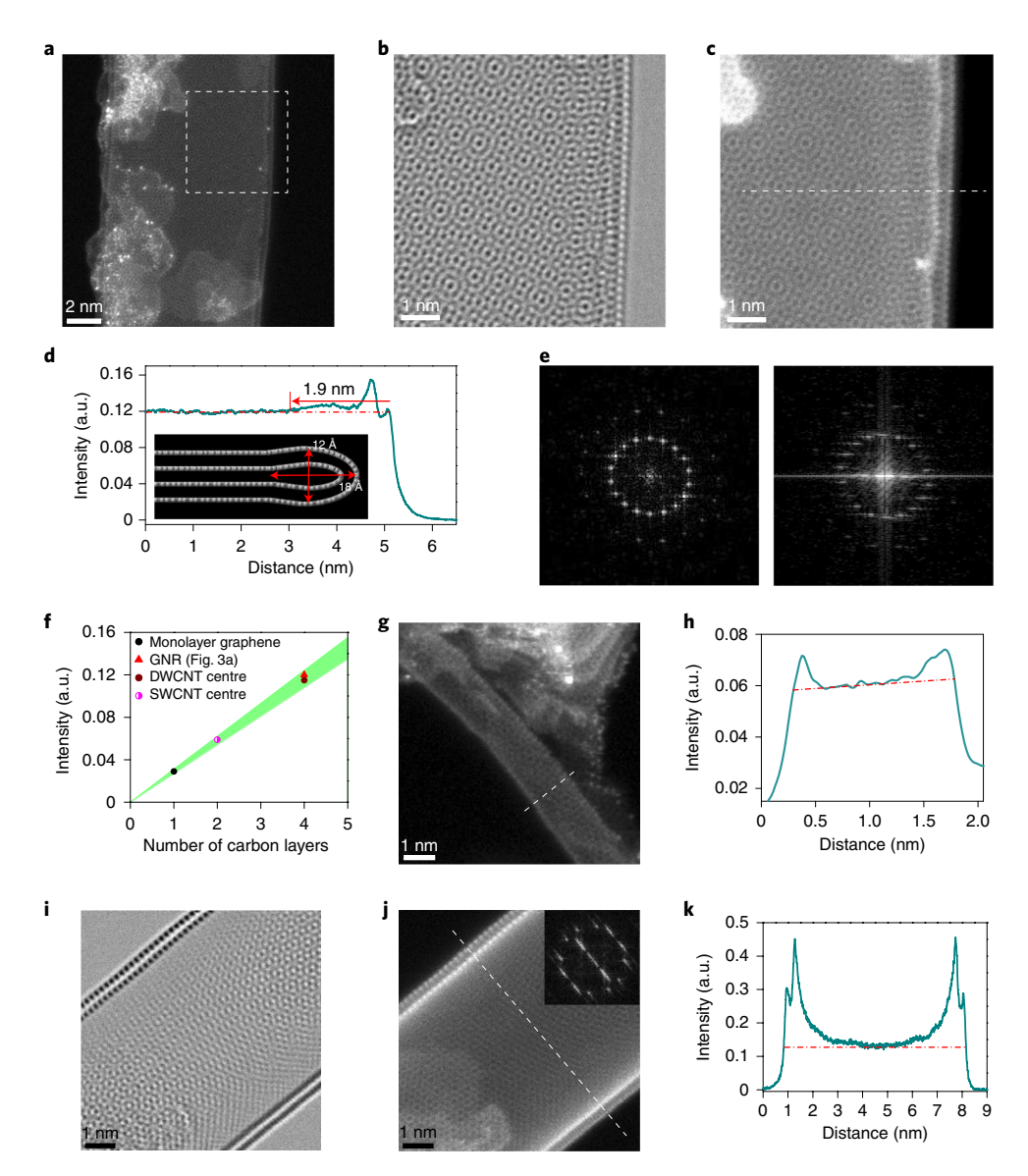


Fig. 3 | High-resolution STEM characterization of GNRs in treated Samples 1 and 2 and a DWCNT. a, STEM-ADF image of a 9.2-nm-wide GNR (Sample 1). **b,c**, Atomic-resolution STEM-BF image (**b**) and STEM-ADF image (**c**) taken simultaneously from the highlighted region (dashed square box) in **a**. **d**, STEM-ADF image intensity profile (an almost constant projected scattering potential) in the central region of the GNR and a higher ADF image intensity in the edge region. Inset: a structural model of a squashed edge-closed GNR, showing a flat plane in the central region of the GNR and a bulb with the oval cross-section in the edge region. **e**, FFT patterns of the BF image taken from the central region (left) and edge region (right) of the GNR in **b**. **f**, STEM-ADF image intensity quantification of the GNR, graphene and CNTs, showing that the GNR in **a** has four layers. The green-shaded region accounts for the intensity variation caused by the change in electron probe current density. **g**, STEM-ADF image of a GNR with a width of 1.4 ± 0.1 nm (Sample 2). **h**, STEM-ADF image intensity profile taken along the white dashed line in **g**. **i,j**, Atomic-resolution STEM-BF (**i**) and STEM-ADF (**j**) image of a DWCNT with a diameter of 7.2 nm. The inset in **j** shows the FFT pattern from the BF image (i) of the CNT, showing streaks at the diffraction spots. **k**, STEM-ADF image intensity profile taken along the white dashed line in **j**, showing a gradual increase in the ADF image intensity from the centre to the edge. The white coating on the GNRs and the CNT in **a**, **g** and **j** is the residual PmPV.

images. The FFT pattern of a GNR from the central region shows sharp diffraction spots (Fig. 3e, left), while the FFT pattern from the edge region has streaks at the diffraction spots (Fig. 3e, right). In contrast, the FFT patterns from both central and edge regions of a CNT show streaks at the diffraction spots (Fig. 3j, inset). This indicates that GNRs have a flat configuration in the central region with slight curvature close to the edges.

The STEM images, image intensity profiles and FFT patterns confirm that the GNR in Fig. 3a is an edge-closed GNR with a flattened central region and two bulbs in the two edge regions. To estimate the height and width of the bulbs, we simulated the STEM-ADF

image and its intensity profile for an edge-closed GNR with a width of 9.2 nm by using different bulb heights and widths in the QSTEM software. The simulation showed that with four graphene layers and an interlayer spacing of 0.34 nm in the central flat region, the calculated image intensity profile of the GNR best matches the experimental value when the height and width of the oval cross-sections of the bulbs in the GNR were 1.2 and 1.8 nm, respectively (Fig. 3d, inset, and Supplementary Fig. 6e–h).

We used the intensity quantification of the STEM-ADF image to analyse the number of layers in the GNR. Using monolayer graphene as a reference, the image intensity from the central region of

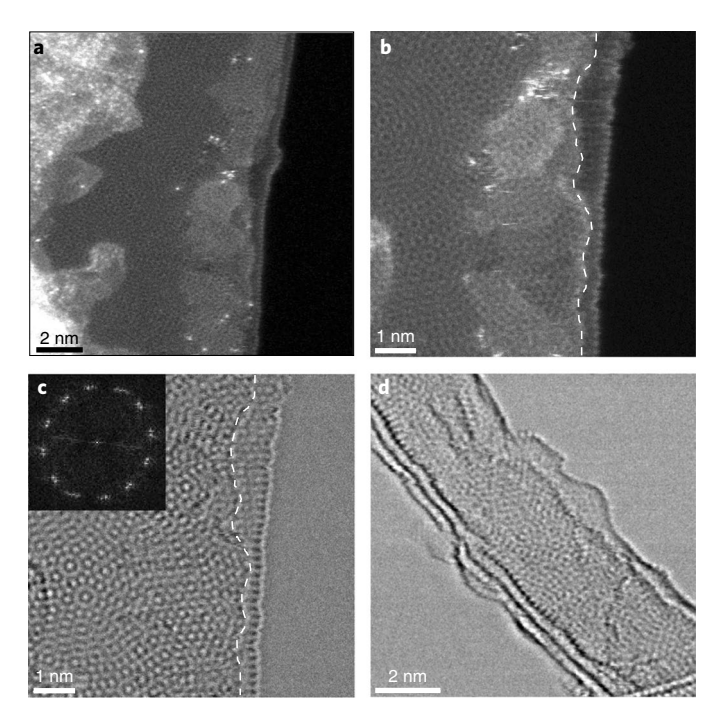


Fig. 4 | Edge-opened GNRs with the edges selectively etched by HNO₃ at high pressure. **a**, STEM-ADF image of a GNR in treated Sample 1, showing the open edge after selective etching. **b**, **c**, Simultaneously acquired zoomed-in STEM-ADF (**b**) and STEM-BF (**c**) images of the GNR in **a**. Inset in **c**: FFT pattern of the BF image taken from the GNR in **c** showing sharp spots, indicating that the GNR is flat. The dashed lines in **b** and **c** indicate the edge of one graphene layer in the double-layer edge-opened GNR. **d**, STEM-BF image of a narrow, edge-opened GNR with a width of 3.3 ± 0.3 nm in treated Sample 2.

the GNR in Fig. 3a was quantified, which also indicated that the GNR had four graphene layers (Fig. 3f). Because the edges of this GNR had two walls, it was confirmed that the GNR was derived from a squashed DWCNT, not an unzipped CNT.

An ultranarrow double-layer GNR with a width down to $1.4\pm0.1\,\mathrm{nm}$ could be observed in treated Sample 2 (Fig. 3g), which is the one of the narrowest GNRs among those prepared by top-down approaches^{5,20,22,23}. Similarly, the image intensity profile of this GNR was nearly flat in the central region with higher intensity at the edges (Fig. 3h). Figure 3h has only one image intensity peak at the edges rather than two peaks with a spacing of ~0.34 nm, as shown in Fig. 3d, from which we could deduce that this GNR was derived from a squashed SWCNT. More GNRs from squashed CNTs in treated Sample 1, including a flat GNR and a twisted GNR, are shown in Supplementary Figs. 7 and 8, respectively.

Edge-opened GNRs prepared by etching edges of squashed CNTs

The edge-opened GNRs were prepared by selectively etching the edges of the squashed CNTs using HNO₃ as the oxidant (see Methods for details). The treated samples were recovered from the DACs and sonicated to disperse in solvents for further characterization. A typical sub-10-nm edge-opened GNR in treated Sample 1 is shown in Fig. 4a. Figure 4b,c shows the simultaneously acquired zoomed-in STEM-ADF and STEM-BF images of the GNR in Fig. 4a, respectively, which demonstrate that the edges have been selectively etched to become open in this GNR. The FFT pattern of the obtained edge-opened GNR shows sharp spots (Fig. 4c, inset), indicating that the resulting GNR is flat. In treated Sample 2, sub-5-nm edge-opened GNRs were prepared. A typical narrow,

edge-opened GNR with a width of $3.3\pm0.3\,\mathrm{nm}$ is shown in Fig. 4d. More STEM-ADF images with FFT patterns of edge-opened GNRs are presented in Supplementary Fig. 9. In contrast, no edge-opened GNRs were found when the sample was not treated with HNO₃ at high pressure.

The mechanism for preparing edge-opened GNRs using a suitable oxidant can be explained as follows. When a high pressure is applied, CNTs are squashed into GNRs with closed edges. The edges of the squashed CNTs are under high strain due to the existence of the edge curvature. This results in the carbon atoms at the edges of the flattened CNTs to have much higher reaction activity with HNO₃ than those at the centre. At an optimized temperature, the carbon atoms at the edge of the squashed CNTs are energetically favoured to react with HNO₃. This causes the selective etching of squashed CNTs to form open edges.

AFM and micro-area Raman analysis of GNRs

The prepared edge-closed GNRs have different AFM height profiles from the CNTs. According to the AFM measurements (see Methods for details), the edges of the obtained GNRs are slightly higher than their centres. For two typical edge-closed GNRs (shown in Fig. 5a and Supplementary Fig. 10e), both their edges are 0.18 nm higher than the centres (Fig. 5b,c and Supplementary Figs. 11 and 12), which is consistent with the simulation result based on the STEM measurement (Fig. 3d). Different from GNRs, the centre of a CNT is the highest in the height profile due to the curvature of the CNT. In the AFM phase images, the GNRs show two bright lines at the edges (Supplementary Fig. 11a), which are not observed in the CNTs.

We investigated the effect of pressure and annealing process on the products recovered from different high-pressure and thermal treatments. Before applying high pressure, the apparent heights of the starting CNTs in Sample 1 were mainly in the range of 2.5-7.0 nm based on the AFM measurements (Supplementary Figs. 13a and 14a). Considering that there was a van der Waals separation of ~0.6 nm between the CNT and substrate, the main diameter range of CNTs was 1.9-6.4 nm. When Sample 1 was treated by the pressure cycle, some CNTs were squashed into GNRs. To better identify GNRs, we only distinguished and counted the GNRs whose apparent heights were lower than 2.1 nm (fewer than or equal to four layers for a GNR) in the AFM measurements for analysis. We observed that the yield of GNRs progressively increased as the maximum applied pressure was increased from 8.0 to 22.8 GPa (Supplementary Fig. 13b-d). As the applied pressure was further increased to 30.6 GPa, the products fractured into shorter segments with an average length of ~300 nm, as shown in Supplementary Fig. 13e. It was also found that the annealing process played an important role in the fabrication of GNRs. Control experiments without annealing showed that the yield of GNRs would significantly decrease. This might be because this annealing process partially relieved the stress accumulated in the squashed CNTs or improved the coupling between the opposing interior layers of the squashed CNTs, which aided in stabilizing and fixating the squashed CNTs.

Supplementary Fig. 10a–e shows the sub-10-nm GNRs with widths ranging from 2.8 to 9.4 nm from recovered Sample 1 treated by a peak pressure of 22.8 GPa without adding HNO₃. In the AFM characterization, we also observed structures where only part of the CNT was squashed into the GNR (Supplementary Fig. 10f), which is consistent with the STEM and TEM data. Supplementary Fig. 10f shows that the GNR segments have a much smaller height than the CNT segment. The GNR was observed to be wider and lower compared with the CNT (Supplementary Fig. 10g). Sub-10-nm double-layer GNRs prepared by treating Sample 1 at the same pressure with added HNO₃ are also shown in Supplementary Fig. 15. Both edge-closed and edge-opened GNRs obtained without and with HNO₃, respectively, have a uniform width along the whole nanoribbon based on the AFM characterization.

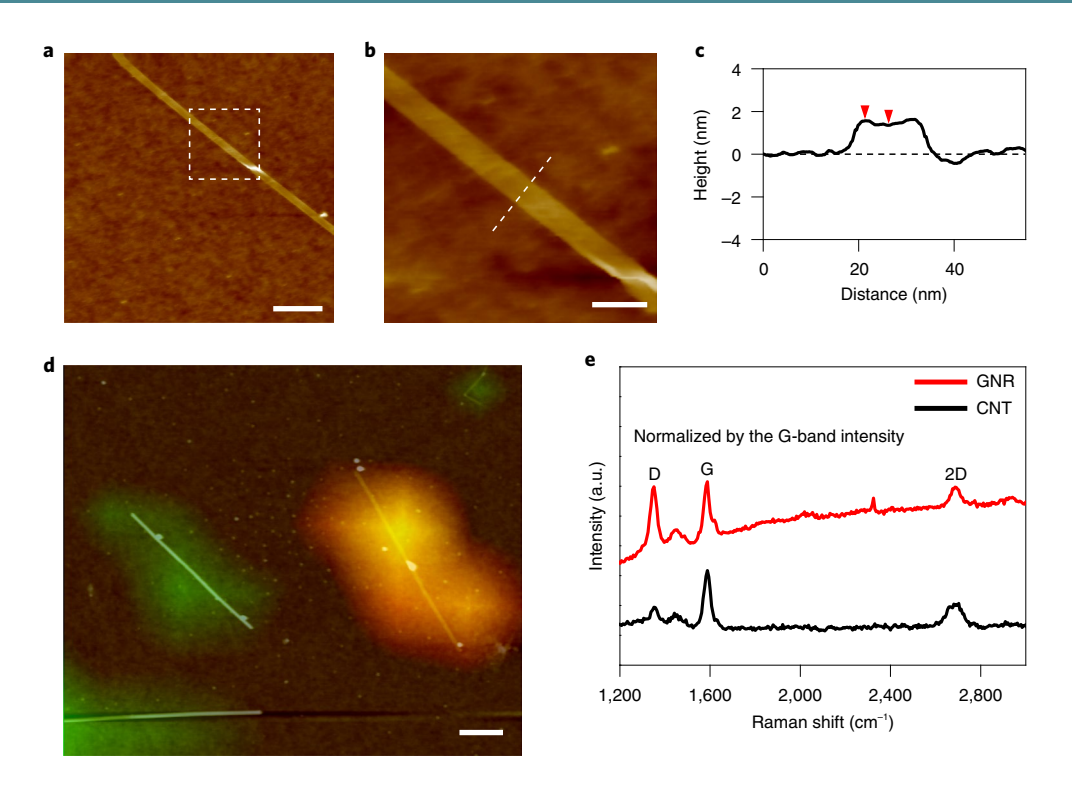


Fig. 5 | AFM images and Raman measurements of edge-closed GNRs from squashed CNTs. **a**, AFM image of a GNR (7.9 nm in width and 1.3 nm in apparent height; double layers). **b**, Zoomed-in AFM image of the highlighted region (dashed square box) in **a**. **c**, Height profile measured along the direction perpendicular to the length direction of the GNR (dashed line) in **b**. Two red arrowheads indicate that the edges of the GNR are 0.18 nm higher than the centre. **d**, Overlay of Raman and AFM images for individual GNR (yellow) and CNTs (green). The Raman image is generated based on the total intensity integrals of the D-band (red) and G-band (green). A GNR that has a relatively high D-to-G intensity ratio is shown as yellow, while CNTs with low D-to-G intensity ratios are shown as green. **e**, Raman spectra taken from the GNR (right) and CNT (left) in **d**. The scale bars in **a**, **b** and **d** are 100, 20 and 200 nm, respectively.

Statistical analysis on the product of Sample 1 treated by a peak pressure of 22.8 GPa without adding HNO₃ showed that the heights of the prepared GNRs were mainly around 1.3 and 1.9 nm (Supplementary Fig. 14b) when only considering GNRs lower than 2.1 nm, which corresponds to double-layer and four-layer GNRs derived from squashed SWCNTs and DWCNTs, respectively. The resulting GNRs in treated Sample 1 have a width mainly ranging from 2.8 to 12.1 nm centred at around 7.8 nm (Supplementary Fig. 14c).

Based on the AFM measurements, the yield of GNRs with a layer number fewer than or equal to four layers was estimated to be 38.0 ± 0.6% for Sample 1 treated by a peak pressure of 22.8 GPa without HNO₃. Considering that 70 ± 5% of Sample 1 was SWCNTs and DWCNTs, the yield for squashing SWCNTs and DWCNTs into GNRs was estimated to be 54%. This yield is significantly higher than that from previous methods capable of preparing high-quality, relatively narrow and long edge-opened GNRs. For example, sonication-assisted unzipping of MWCNTs¹⁵ and sonochemical exfoliation of expandable graphite⁶ reported a yield of ~2% and <0.5%, respectively. Unzipping of MWCNTs by plasma etching had a yield of ~20%, but only a very small quantity of MWCNTs spin-coated on the silicon (Si) substrate can be used as the starting material for preparing GNRs in every single batch⁷.

Micro-area Raman mapping was also performed to characterize individual GNRs and CNTs in treated Sample 1 without adding HNO₃ (Methods). An overlay of the Raman image with the AFM image showed excellent consistency (Fig. 5d). This colour-coded Raman image that included an individual GNR and a few CNTs was plotted using the total intensity integrals of the D-band and G-band, which were denoted using red and green, respectively.

Due to a higher D-to-G intensity ratio in a GNR than a CNT, the GNR in Fig. 5d showed as yellow, while the CNTs were green. The higher D-to-G intensity ratio of an edge-closed GNR in comparison to that of a CNT (Fig. 5d,e) is mainly attributed to the presence of edges in the GNR. We also conducted micro-area Raman mapping of an individual GNR and CNT for treated Sample 1 with HNO₃ added to selectively etch the edges of the GNRs (Supplementary Fig. 16). The D-to-G intensity ratio of the GNR in the HNO₃-added sample is much higher than that in the sample without HNO₃. This is because the defects were produced at the open edges with HNO₃ treatment, as confirmed by the STEM characterization.

Electrical measurements and analysis of the as-prepared GNRs

GNR field-effect transistors (GNRFETs) were fabricated with the prepared GNRs on Si wafers with 330-nm-thick thermally oxidized silicon dioxide (SiO₂) (Methods provides the details). Figure 6a shows an overlaid picture of the Raman and AFM image for a typical GNRFET fabricated using an edge-closed GNR from a squashed DWCNT that was $2.8\pm0.5\,\mathrm{nm}$ in width and $2.0\,\mathrm{nm}$ in apparent height (four layers). Raman mapping of the device was conducted after the electrical measurement. A larger D-to-G intensity ratio of the GNR channel (Fig. 6a) relative to that of the pristine CNT sample was observed in the Raman spectrum (Fig. 6b), which is typical for a GNR obtained from a squashed CNT. The output (Fig. 6c) and transfer (Fig. 6d) characteristics of the GNRFET show that the device is a p-type GNRFET. The on-state channel conductance (*G*) normalized by the width of the GNR (*w*) for the device is 10.3 S mm⁻¹. Further, the on-state conductivity of the GNR channel is calculated to be $\sigma = GL/w = 7.42$ mS, where *L* is the channel length.

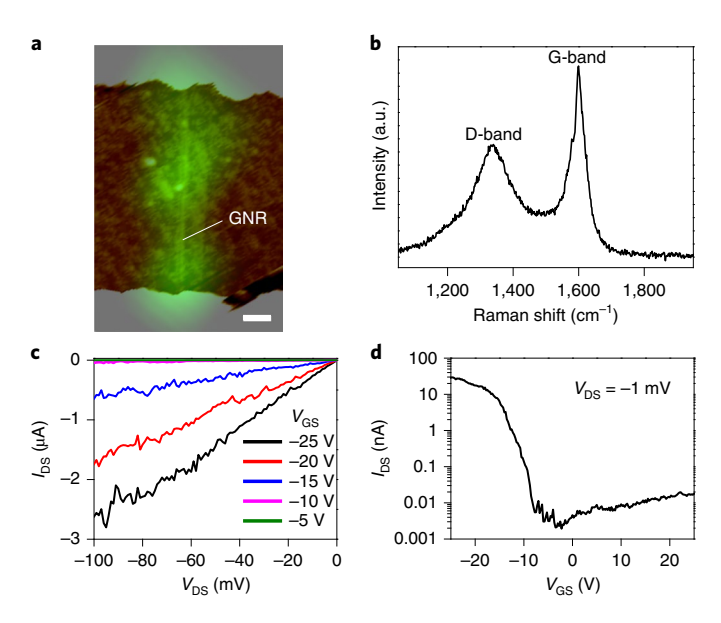


Fig. 6 | Room-temperature electrical measurements of an edge-closed GNR from a squashed DWCNT. a, Overlay of Raman and AFM images for a GNRFET. The Raman image is generated from the intensity integral of the GNR's G-band in green. The GNR is 2.8 nm in width and 2.0 nm in apparent height (four layers). The length of the GNR channel in the GNRFET is 720 nm. Scale bar, 100 nm. **b**, Raman spectrum of the GNR channel in the GNRFET in **a. c.d.** Output (**c**) and transfer (**d**) characteristics of the GNRFET in **a** at room temperature.

The GNRFET was switched off when the gate–source voltage ($V_{\rm GS}$) was larger than $-10\,\rm V$ and had a high $I_{\rm on}/I_{\rm off}$ ratio of 1.5×10^4 as the drain–source voltage ($V_{\rm DS}$) was equal to $-1\,\rm mV$ (Fig. 6d).

If we assume that the fabricated GNR is an intrinsic semiconductor and has a mid-gap line-up with the source/drain metal, then the minimum current (off current) for a GNRFET will occur when both conduction and valence band are flat. The $I_{\rm on}/I_{\rm off}$ ratio at the high-temperature stage (at the stage of thermal carrier emission) will have an exponential dependence on the temperature: $I_{\rm on}/I_{\rm off} \propto \exp[E_{\rm g}/I_{\rm off}]$ $(2k_BT)$], where E_g , k_B and T are the bandgap, Boltzmann constant and temperature, respectively 10,44. Thus, a bandgap of ~494 meV is estimated for this GNR. This bandgap is substantially larger than that of the GNR derived from unzipped CNT in our earlier work, which was only 10-15 meV (ref. 15), because narrower GNRs were prepared with the present method. In addition, we also find the I_{on}/I_{off} ratio of GNRFETs and bandgap of GNRs decrease as the width of the prepared GNRs increases. For a GNRFET fabricated with a 7.1-nm-wide 1.9-nm-high (four layers) GNR (Supplementary Fig. 17), an I_{on}/I_{off} ratio of ~110 is obtained (Supplementary Fig. 17e) and a bandgap of 161 meV is extracted for the GNR channel from the temperature-dependent electrical measurements (Supplementary Fig. 17f,g) based on the dependence of minimum conductance on temperature at the high-temperature stage: $G_{\text{off}} \propto \exp[-E_e/(2k_BT)]$. For a GNRFET fabricated with a 11.5-nm-wide 1.9-nm-high GNR (Supplementary Fig. 18), the $I_{\rm on}/I_{\rm off}$ ratio is ~10 (Supplementary Fig. 18d) and a bandgap of 63 meV is extracted for the GNR channel (Supplementary Fig. 18e, f). Possible errors in our E_g versus w analysis include uncertainties in w based on the AFM measurements and in the assumption of the same Schottky barrier height for electrons and holes in GNRFETs. It is found that the bandgap values extracted from edge-closed GNRs of different widths approximately conform to a formula of E_{α} (meV) = 891/[w (nm) – 1.0].

To better understand the properties of the GNR from squashed CNTs, we also calculated the theoretical bandgap and band structure of a circular (10, 10) SWCNT and a double-layer GNR from

squashed (10, 10) SWCNT via ab initio density functional theory calculations (Supplementary Fig. 19a-e). The calculations showed that the edge-closed GNR consists of a central flat region where two opposing walls are flattened and stabilized due to the van der Waals interaction and two strained bulbs with elliptical cross-sections at the two edges. The simulated height of the bulbs and interlayer spacing in the central region for the GNR were about 0.56 and 0.34 nm, respectively. It is predicted that the shape and size of the edge bulbs have an effect on the bandgap of the prepared edge-closed GNR because they would affect the width of the GNR. Our calculations showed that a bandgap of ~0.2 eV can open when the sample structure varied from the circular (10, 10) SWCNT with zero bandgap to the edge-closed GNR, which was also confirmed by the tight-binding calculation (Supplementary Fig. 19f). The result confirmed that metallic armchair CNTs can be transformed into semiconductors by squashing CNTs into GNRs, which was consistent with previous theoretical results^{45,46}. An earlier theoretical investigation showed the opening of bandgaps for both armchair and zigzag collapsed nanotubes due to quantum confinement and charge transfer between the flat central region and strained edge bulbs⁴⁶. Both armchair and zigzag collapsed nanotubes show an inverse relation between the calculated bandgap and collapsed nanotube width. Different from armchair collapsed CNTs, zigzag collapsed nanotubes can be classified into three semiconductor families that have distinct scaling rules for the bandgap versus collapsed nanotube width.

The field-effect mobility of GNRFETs was also calculated based on the formula $\mu = g_{\rm m} L^2 / (C_{\rm gs} V_{\rm ds})$, where $g_{\rm m}$ is the transconductance of the device and $C_{\rm gs}$ is the gate capacitance. A three-dimensional electrostatic simulation was used to calculate the $C_{\rm gs}$ of the GNRFET, as described in Supplementary Note 3 (ref. 5). For the 2.8-nm-wide GNR (Fig. 6a), $C_{\rm gs}$ was calculated to be 6.6 aF. Thus, the hole field-effect mobility (μ) of the device was calculated to be $2,443 \text{ cm}^2 \text{ V}^{-1} \text{ s}^{-1}$, which is the highest among GNRFETs with similar widths of GNR channels reported so far^{5–7,42,47–49}. This device shows more than one order of magnitude higher mobility and nearly two orders of magnitude higher on-state channel conductivity compared with FETs based on the sub-10-nm edge-opened GNRs prepared by sonicating exfoliated expandable graphite⁶, while $I_{on}/I_{off} > 10^4$ can be obtained for both GNRFETs (Supplementary Table 1). Therefore, large I_{on}/I_{off} ratio and device mobility can be simultaneously achieved in the FET fabricated with narrow edge-closed GNR. In contrast, the GNRFETs in earlier reports either did not present good mobilities^{42,47} or I_{on}/I_{off} ratios^{15,16,50}, or a combination of these characteristics^{48,49}. Similarly, for the four-layer edge-closed GNR with a 7.1 nm width (Supplementary Fig. 17), $C_{\rm gs}$ and μ were calculated to be 2.6 aF and 1,609 cm² V⁻¹ s⁻¹, respectively. For the four-layer edge-closed GNR with a width of 9.9 nm (Supplementary Fig. 20), $C_{\rm gs}$ and μ were calculated to be 1.7 aF and 3,776 cm² V⁻¹ s⁻¹, respectively. This device mobility is one of the highest values among GNRFETs fabricated by GNRs with a width narrower than 20 nm (refs. 5-7,15,16,42,47-50). Our GNRFET fabricated by the 2.8-nm-wide GNR exhibits a higher on-state channel conductivity and better comprehensive device performance (I_{on}/I_{off} ratio, on-state channel conductivity and mobility) than previously reported FETs fabricated by GNRs with open edges and by semiconducting SWCNTs with different diameters (Supplementary Table 1)5-7,15,16,42,47-50. We also measured two other FETs fabricated by edge-closed GNRs with a width of ~2.9 nm and similar $I_{\rm on}/I_{\rm off}$ ratios and mobilities were observed. The device mobility and on-state channel conductivity confirm the high quality of the prepared GNRs with atomically smooth closed edges.

Conclusions

We have shown that sub-10-nm-wide, long semiconducting GNRs with closed edges can be produced by irreversibly squashing CNTs

using a high-pressure and thermal treatment. The GNRs obtained from squashed CNTs have atomically smooth, closed edges and few defects. Sub-5-nm GNRs could be created, with a minimum width of 1.4 nm. For CNTs with diameters in the range of 1.9-6.4 nm, 54% of the SWCNTs/DWCNTs present in the sample became two- or four-layer-thick GNRs using this method. Edge-opened GNRs could also be prepared by using a suitable oxidant (HNO₃) to selectively etch the edges of the squashed CNTs under high pressure. An FET with a 2.8-nm-wide edge-closed GNR exhibits a high $I_{\rm on}/I_{\rm off}$ ratio of >10⁴, field-effect mobility of 2,443 cm² V⁻¹ s⁻¹ and on-state channel conductivity of 7.42 mS. A bandgap of around 494 meV is estimated for this GNR. Our approach provides a route to fabricate narrow and long GNRs with smooth edges, sizeable bandgaps and high mobilities, and also provides guidance for controlling the edge types for exploring their fundamental properties and practical application in electronics and optoelectronics. The method could be extended to other fullerenes and materials that form nanotubes.

Methods

Sample purification. Sample 1 was purified as follows. The pristine sample was heated to 400 °C in air for 45 min to oxidize the catalytic iron nanoparticles. After air oxidation, the sample was further heat-treated at 800 °C for 60 min under an argon atmosphere to remove the graphitic shells on the catalysts by its reaction with the encapsulated iron oxide at high temperature. Then, the sample was refluxed in 12 M HCl at 100 °C for 4h. The sample, after acid treatment, was filtered and rinsed with distilled water, followed by drying under a vacuum. In the resulting sample, $70\pm5\%$ of the CNTs were composed of SWCNTs and DWCNTs, while the remaining were few-walled CNTs with number of walls higher than two.

Sample 2 was purified by air oxidation and HCl reaction. First, 1 g CNT sample was calcined at 500 °C in air for 1 h to remove the amorphous carbon impurity. The resulting sample was added into the mixture of 20 ml HCl (37% w/w) and 20 ml deionized water, and the obtained solution was sonicated for 1 h to remove the metal catalysts in the sample. Then, the sample was filtered and rinsed with deionized water. The wet, as-filtered CNTs were then fully dispersed in deionized water by sonicating the solution for 45 min. Finally, the resulting solution was lyophilized under a vacuum to avoid the agglomeration of CNTs.

Preparation of edge-closed and edge-opened GNRs. The high-pressure experiments were conducted using symmetric DACs with 600- μ m-diameter diamond culets. Sample chambers (410 μ m in diameter and 70 μ m in height) were drilled at the centre of tungsten gaskets pre-indented to about 13 GPa. These chambers were used for loading the CNT samples along with a ruby sphere as a pressure calibrant 51 . The enclosed CNT samples filling the sample chambers were gradually compressed between two diamond anvils up to the target pressures. To stabilize the squashed sample structure for preventing reversible structural transition on decompression or selectively etch the edges of the squashed CNTs, thermal treatment was conducted on the samples at the highest applied pressure. We performed a set of control experiments to find the optimal pressures and thermal treatment processes to produce high-quality GNRs with high yield.

In the case of preparing edge-closed GNRs, purified Sample 1 or 2 was loaded into the DAC chamber using a tungsten needle to transfer the flocculent CNTs until the sample chamber of the DAC was fully packed. Pressures up to 22.8 and 28.1 GPa were gradually applied to compress Samples 1 and 2, respectively. At the highest pressure, the DAC enclosed with the samples was heated up to 220 °C in a furnace and held at that temperature for 40 min for thermal treatment. In the case of preparing edge-opened GNRs, purified Sample 1 or Sample 2 (0.4 mg) was sonicated in $300\,\mu l$ HNO₃ (69% w/w) for 15 min. The resulting wet mixture of CNTs and HNO3 were transferred and loaded into the DAC chamber by using a tungsten needle or a micro-syringe to fill the chamber. Pressures up to 22.4 and 27.9 GPa were applied to Samples 1 and 2, respectively, with HNO3 oxidant in the DAC. The DAC was then heated up to 220 °C and kept for 40 min at the peak pressure to allow the edges of squashed CNTs to selectively react with the HNO3 oxidant. Afterwards, the DACs for preparing edge-closed and edge-opened GNRs were cooled down to room temperature under a rapid airflow, followed by gradual and slow decompression to ambient pressure. The resulting samples were recovered from the DACs and sonicated to disperse in solvents. Treated Sample 1 was sonicated in 200 μ l of 1,2-dichloroethane (DCE) solution with poly(m-phenylenevinylene-co-2,5-dioctoxy-p-phenylenevinylene) (PmPV) (1.9 mg ml⁻¹) as the surfactant for $30\,min$, and treated Sample 2 was sonicated in a mixture of $100\,\mu l$ PmPV/DCE $(1.9\,\mathrm{mg\,ml^{-1}})$ and $100\,\mu\mathrm{l}$ dimethylformamide for $30\,\mathrm{min}$. The resulting solutions were diluted in several millilitres of PmPV/DCE (1.9 mg ml-1) for further characterization and device fabrication.

In situ high-pressure Raman measurement. Raman measurements used a Horiba–Jobin–Yvon LabRAM HR confocal Raman system and a Renishaw inVia confocal Raman system. A 532 nm helium–neon excitation laser was used in both systems. In situ Raman measurements were conducted along the compression and decompression processes. The diamond anvil acted as an optical window through which the samples were excited and Raman scattering signals were collected. To analyse the samples without the effect of the diamond window on the Raman D-band and examine the D-to-G intensity ratio, we also collected the Raman spectra of the samples in the chamber with the DAC opened before loading the pressure and after releasing the pressure, respectively.

TEM and STEM characterizations of GNRs. The samples were prepared by dropping diluted GNR solutions onto TEM grids, which were laid on a piece of filter paper. The TEM grids were lacey carbon-coated 200 mesh gold grids (SPI Supplies) or a QUANTIFOIL substrate with a carbon film mounted on a 300 mesh gold grid, which has an orthogonal array of 1.2-μm-diameter circular holes with 1.3 μm separation (Ted Pella). The resulting TEM grids were dipped and rinsed in DCE for 10 min. TEM observation and imaging of the samples were performed on an FEI Tecnai G2 F20 X-TWIN instrument.

STEM-ADF imaging was performed on an aberration-corrected Nion UltraSTEM 100 instrument operating at 60 kV. The convergence semi-angle for the incident probe was set to be 31 mrad. The ADF images were collected for a half-angle range of 86–200 mrad, and the BF images were simultaneously collected with ADF images for a half-angle range of 0–10 mrad. The STEM images were only low-pass filtered to reduce random noise in the images.

Simulation of scattering potentials and ADF image intensities of GNRs and CNTs. The scattering potentials of DWCNT and four-layer edge-closed GNRs were calculated using the QSTEM 2.30 software (http://qstem.org/). The STEM-ADF image simulation was performed using the same software with the parameters (accelerating voltage, probe convergence angle, detector angle and third-order aberration) comparable with the experimental conditions. The simulated images were convolved with a Gaussian of 1 Å to account for the effects from other aberrations.

AFM characterization of GNRs. The products were spin-coated onto $1 \times 1 \, \mathrm{cm^2}$ SiO₂/Si wafers at 1,500 r.p.m. for 1 min followed by heating at 80 °C for 2 min in a drying oven to fixate the GNRs. The substrates were then successively rinsed with DCE and isopropanol to remove most of the PmPV and then blow-dried. The resulting samples were calcined in air at 350 °C for 20 min to further remove any remaining PmPV. The samples were observed using a Dimension 3100 scanning probe microscope in the tapping mode. Commercial AFM tips (AppNano, model no. ACST; force constant, $k = 7 \, \mathrm{N \, m^{-1}}$, and resonance frequency, $f_0 = 150 \, \mathrm{kHz}$) were used. The width, height and surface morphology of the GNRs were recorded. To obtain a more accurate GNR width, the same tips were used to measure the apparent width of the HiPCO SWCNTs with a specific diameter (Carbon Nanotechnologies) to deduce the effect of the AFM tip size on the width measurement. According to our measurement, the actual width of a GNR was about 7 nm less than the measured apparent width while the effect of the AFM tip size was corrected.

Raman mapping of individual GNRs and CNTs. The positions of individual GNRs and CNTs on the SiO₂/Si wafers relative to pre-patterned markers were measured via AFM. A Horiba–Jobin–Yvon LabRAM HR confocal Raman system was used for Raman mapping. A 532-nm helium–neon laser was used as the excitation light, and it had a spot size of 0.6 μ m under ×100 objective and a light intensity of ~1 mW μ m $^{-2}$. The substrate with GNRs and CNTs was first observed under a Raman microscope to assure the relative location of the GNR or CNT via the markers. We made a Raman map over an area of $4\times4\,\mu$ m 2 . Here a confocal hole diameter of $150\,\mu$ m, slit width of $100\,\mu$ m and typical exposure integration time of ~40 s per spot were used.

Fabrication of GNRFETs and electrical measurements. The products were spin-coated onto Si wafers with 330-nm-thick thermally oxidized SiO₂ and then treated to remove the PmPV, as described in the AFM characterization. GNRs fewer than or equal to four layers were identified by the AFM measurement for device fabrication. To construct the GNRFETs, parallel palladium electrodes (30 nm thick) were fabricated onto the GNRs by electron-beam lithography and lift-off technique to act as the source and drain of the device. The GNR between the source and drain acted as the channel, and Si substrate was used as the back gate. The devices were then annealed at 200 °C for 20 min in a vacuum to improve the contacts. An Agilent 4156C semiconductor parameter analyser was used to measure the devices in a vacuum at 6 × 10 $^{-6}$ torr. A Janis closed-cycle helium cryostat was used to cool down the devices to conduct the temperature-dependent electrical measurements from 295 to 5 K.

Data availability

The data that support the plots within this paper and other findings of this study are available from the corresponding authors upon reasonable request.

Received: 20 December 2020; Accepted: 19 July 2021; Published online: 6 September 2021

References

- 1. Schwierz, F. Graphene transistors. Nat. Nanotechnol. 5, 487-496 (2010).
- Yazyev, O. V. A guide to the design of electronic properties of graphene nanoribbons. Acc. Chem. Res. 46, 2319–2328 (2013).
- Yang, L., Park, C. H., Son, Y. W., Cohen, M. L. & Louie, S. G. Quasiparticle energies and band gaps in graphene nanoribbons. *Phys. Rev. Lett.* 99, 186801 (2007).
- Son, Y. W., Cohen, M. L. & Louie, S. G. Energy gaps in graphene nanoribbons. Phys. Rev. Lett. 97, 216803 (2006).
- Wang, X. R. et al. Room-temperature all-semiconducting sub-10-nm graphene nanoribbon field-effect transistors. *Phys. Rev. Lett.* 100, 206803 (2008).
- Li, X. L., Wang, X. R., Zhang, L., Lee, S. W. & Dai, H. J. Chemically derived, ultrasmooth graphene nanoribbon semiconductors. *Science* 319, 1229–1232 (2008).
- Jiao, L. Y., Zhang, L., Wang, X. R., Diankov, G. & Dai, H. J. Narrow graphene nanoribbons from carbon nanotubes. *Nature* 458, 877–880 (2009).
- 8. Kimouche, A. et al. Ultra-narrow metallic armchair graphene nanoribbons. *Nat. Commun.* **6**, 10177 (2015).
- Ma, C. X. et al. Seamless staircase electrical contact to semiconducting graphene nanoribbons. Nano Lett. 17, 6241–6247 (2017).
- Chen, C. X. et al. Graphene nanoribbons under mechanical strain. Adv. Mater. 27, 303–309 (2015).
- Xie, L. M. et al. Graphene nanoribbons from unzipped carbon nanotubes: atomic structures, Raman spectroscopy, and electrical properties. *J. Am. Chem. Soc.* 133, 10394–10397 (2011).
- Fang, T., Konar, A., Xing, H. L. & Jena, D. Mobility in semiconducting graphene nanoribbons: phonon, impurity, and edge roughness scattering. *Phys. Rev. B* 78, 205403 (2008).
- Basu, D., Gilbert, M. J., Register, L. F., Banerjee, S. K. & MacDonald, A. H. Effect of edge roughness on electronic transport in graphene nanoribbon channel metal-oxide-semiconductor field-effect transistors. *Appl. Phys. Lett.* 92, 042114 (2008).
- Han, M. Y., Ozyilmaz, B., Zhang, Y. B. & Kim, P. Energy band-gap engineering of graphene nanoribbons. *Phys. Rev. Lett.* 98, 206805 (2007).
- Jiao, L. Y., Wang, X. R., Diankov, G., Wang, H. L. & Dai, H. J. Facile synthesis of high-quality graphene nanoribbons. *Nat. Nanotechnol.* 5, 321–325 (2010).
- Wang, X. R. et al. Graphene nanoribbons with smooth edges behave as quantum wires. Nat. Nanotechnol. 6, 563–567 (2011).
- Kosynkin, D. V. et al. Longitudinal unzipping of carbon nanotubes to form graphene nanoribbons. *Nature* 458, 872–876 (2009).
- Pan, M. H. et al. Topographic and spectroscopic characterization of electronic edge states in CVD grown graphene nanoribbons. *Nano Lett.* 12, 1928–1933 (2012).
- Oliveira, M. H. et al. Synthesis of quasi-free-standing bilayer graphene nanoribbons on SiC surfaces. Nat. Commun. 6, 7632 (2015).
- Wang, X. R. & Dai, H. J. Etching and narrowing of graphene from the edges. Nat. Chem. 2, 661–665 (2010).
- 21. Bai, J. W., Duan, X. F. & Huang, Y. Rational fabrication of graphene nanoribbons using a nanowire etch mask. *Nano Lett.* **9**, 2083–2087 (2009).
- Yu, F. et al. Controlled fabrication of intermolecular junctions of single-walled carbon nanotube/graphene nanoribbon. *Small* 9, 2405–2409 (2013).
- Magda, G. Z. et al. Room-temperature magnetic order on zigzag edges of narrow graphene nanoribbons. Nature 514, 608–611 (2014).
- Yang, W. L., Lucotti, A., Tommasini, M. & Chalifoux, W. A. Bottom-up synthesis of soluble and narrow graphene nanoribbons using alkyne benzannulations. J. Am. Chem. Soc. 138, 9137–9144 (2016).
- Narita, A. et al. Synthesis of structurally well-defined and liquid-phaseprocessable graphene nanoribbons. Nat. Chem. 6, 126–132 (2014).
- Grosse, K. L., Bae, M. H., Lian, F. F., Pop, E. & King, W. P. Nanoscale Joule heating, Peltier cooling and current crowding at graphene–metal contacts. *Nat. Nanotechnol.* 6, 287–290 (2011).
- Xia, F. N., Perebeinos, V., Lin, Y.-M., Wu, Y. Q. & Avouris, P. The origins and limits of metal-graphene junction resistance. *Nat. Nanotechnol.* 6, 179–184 (2011).
- Huang, B.-C., Zhang, M., Wang, Y. J. & Woo, J. Contact resistance in top-gated graphene field-effect transistors. *Appl. Phys. Lett.* 99, 032107 (2011).
- Cai, J. M. et al. Atomically precise bottom-up fabrication of graphene nanoribbons. *Nature* 466, 470–473 (2010).
- Ruffieux, P. et al. On-surface synthesis of graphene nanoribbons with zigzag edge topology. Nature 531, 489–492 (2016).
- Jacobse, P. H. et al. Electronic components embedded in a single graphene nanoribbon. Nat. Commun. 8, 119 (2017).

 Kolmer, M. et al. Rational synthesis of atomically precise graphene nanoribbons directly on metal oxide surfaces. Science 369, 571–575 (2020).

- Ma, J., Wang, J. N. & Wang, X. X. Large-diameter and water-dispersible single-walled carbon nanotubes: synthesis, characterization and applications. J. Mater. Chem. 19, 3033–3041 (2009).
- Qi, H., Qian, C. & Liu, J. Synthesis of high-purity few-walled carbon nanotubes from ethanol/methanol mixture. *Chem. Mater.* 18, 5691–5695 (2006).
- Liew, K. M. & Sun, Y. Z. Elastic properties and pressure-induced structural transitions of single-walled carbon nanotubes. *Phys. Rev. B* 77, 205437 (2008).
- Elliott, J. A., Sandler, J. K. W., Windle, A. H., Young, R. J. & Shaffer, M. S. P. Collapse of single-wall carbon nanotubes is diameter dependent. *Phys. Rev. Lett.* 92, 095501 (2004).
- Mu, W. H., Cao, J. S. & Ou-Yang, Z. C. Shape transition of unstrained flattest single-walled carbon nanotubes under pressure. J. Appl. Phys. 115, 044512 (2014).
- Gillen, R., Mohr, M., Thomsen, C. & Maultzsch, J. Vibrational properties of graphene nanoribbons by first-principles calculations. *Phys. Rev. B* 80, 115418 (2009).
- Talirz, L. et al. On-surface synthesis and characterization of 9-atom wide armchair graphene nanoribbons. ACS Nano 11, 1380 (2017).
- Peköz, R., Feng, X. L. & Donadio, D. Ab initio characterization of graphene nanoribbons and their polymer precursors. *J. Phys.: Condens. Matter* 24, 104023 (2012).
- Borin, B. G. et al. Surface-synthesized graphene nanoribbons for room temperature switching devices: substrate transfer and ex situ characterization. ACS Appl. Nano Mater. 2, 2184–2192 (2019).
- Fairbrother, A. et al. High vacuum synthesis and ambient stability of bottom-up graphene nanoribbons. Nanoscale 9, 2785–2792 (2017).
- Sanders, G. D., Nugraha, A. R. T., Saito, R. & Stanton, C. J. Coherent radial-breathing-like phonons in graphene nanoribbons. *Phys. Rev. B* 85, 205401 (2012).
- 44. Chen, Z. H., Lin, Y.-M., Rooks, M. J. & Avouris, P. Graphene nano-ribbon electronics. *Phys. E* 40, 228–232 (2007).
- Pantano, A. Effects of mechanical deformation on electronic transport through multiwall carbon nanotubes. *Int. J. Solids Struct.* 122–123, 33–41 (2017).
- Impellizzeri, A., Briddon, P. & Ewels, C. P. Stacking- and chirality-dependent collapse of single-walled carbon nanotubes: a large-scale density-functional study. *Phys. Rev. B* 100, 115410 (2019).
- 47. Llinas, J. P. et al. Short-channel field-effect transistors with 9-atom and 13-atom wide graphene nanoribbons. *Nat. Commun.* **8**, 633 (2017).
- Murakami, K. et al. Synthesis of graphene nanoribbons from amyloid templates by gallium vapor-assisted solid-phase graphitization. Appl. Phys. Lett. 104, 243101 (2014).
- Jordan, R. S. et al. Synthesis of graphene nanoribbons via the topochemical polymerization and subsequent aromatization of a diacetylene precursor. *Chem* 1, 78–90 (2016).
- Hwang, W. S. et al. Graphene nanoribbon field-effect transistors on wafer-scale epitaxial graphene on SiC substrates. APL Mater. 3, 011101 (2015).
- 51. Mao, H., Xu, J. & Bell, P. M. Calibration of the ruby pressure gauge to 800 kbar under quasi-hydrostatic conditions. *J. Geophys. Res. B* **91**, 4673 (1986).

Acknowledgements

C.C. acknowledges support from the National Natural Science Foundation of China for Excellent Young Scholars (no. 61622404), Chang Jiang (Cheung Kong) Scholars Program of Ministry of Education of China (no. Q2017081), National Natural Science Foundation of China (no. 62074098) and Science and Technology Innovation Action Program from the Science and Technology Commission of Shanghai Municipality (no. 15520720200). Y.L., W.L.M. and the high-pressure DAC experiments were supported by the United States Department of Energy through the Stanford Institute for Materials and Energy Sciences DE-AC02-76SF00515. Work by J.N.W. was supported by the National Key R&D Program of China (2018YFA0208404) and Innovation Program of Shanghai Municipal Education Commission. J.G. was supported by NSF grant nos. 1809770 and 1904580. Work at ORNL was supported by the US Department of Energy, Office of Science, Basic Energy Sciences, Materials Sciences and Engineering Division. W.Z. acknowledges support from the Beijing Outstanding Young Scientist Program (BJJWZYJH01201914430039).

Author contributions

H.D. and C.C. conceived and designed the experiments and C.C. conceived the theoretical calculations and simulations. C.C. planned and supervised the project. C.C., Y.L., W.Z., M.G., Z.H., E.S., X.L., J.Z.W., J.N.W., F.Y., Q.Z., J.L., G.H., A.L.A. and M.-C.L. performed the experiments and prepared the pristine CNT samples. C.C., Z.H., K.T.L., J.G., W.G. and J.-M.Z. performed the numerical simulations. C.C., Y.L., W.Z., M.G., Z.H., F.S., X.L., J.Z.W., K.T.L., F.Y., Q.Z., J.G., W.G., J.-M.Z., G.H., W.L.M. and H.D. analysed

the data and wrote the manuscript. All the authors discussed the results and commented on the manuscript.

Competing interests

The authors declare no competing interests.

Additional information

Supplementary information The online version contains supplementary material available at https://doi.org/10.1038/s41928-021-00633-6.

Correspondence and requests for materials should be addressed to Changxin Chen, Wendy L. Mao or Hongjie Dai.

An-Ping Li for their contribution to the peer review of this work.

Peer review information Nature Electronics thanks Antonio Pantano, Chee-Tat Toh and

Reprints and permissions information is available at www.nature.com/reprints.

Publisher's note Springer Nature remains neutral with regard to jurisdictional claims in published maps and institutional affiliations.

© The Author(s), under exclusive licence to Springer Nature Limited 2021